

Multi-phase welding simulation, experimental validation and exploratory bending simulation of structural steel weldments

Tobias Girresser¹, Tobias Loose²

¹Technologie-Institut für Metall und Engineering GmbH

²Dr. Loose GmbH

1 Abstract

To predict the load-bearing capacity of a welded joint, it is necessary to know the structure that will be formed. In recent decades, welding simulation has evolved and now offers the possibility to determine the required material properties after welding [1]. Computational welding mechanics (CWM) is a calculation method that can be used to calculate distortions, mechanical stresses, and strains as well as microstructure states and microstructure transformations in thermally joined components [2, 3].

The material models for CWM consider several phases, but not descriptions of the damage. The material model developed by [4], which is specially tailored to the requirements of welding and heat treatment simulation, is available as keyword `*MAT_GENERALIZED_PHASE_CHANGE (*MAT_254)`. It contains, among other things, the calculation of the microstructure evolution of up to 24 individual phases, whereby various phase change mechanisms are integrated for the phase transformations (e.g., Leblond, JMAK, Koistinen-Marburger, Kirkaldy). In welding simulation, the processes associated with phase transformations: heating, cooling and reheating in multi-layer weld seams, including the tempering effect, can thus be modeled.

For crash simulations, in which limit load capacities are also determined, the states calculated with CWM represent a starting point but cannot yet be used because the single-phase material models of the crash simulation are often inconsistent with CWM. This leads to uncertainties in the simulation results, especially in the prediction of load-bearing capacities.

In this talk, CWM with the material model `*MAT_254`, validation experiments and a virtual damage study of weldments will be presented. The software FabWeld® [5] is used to pre-process the welding simulation and processes the temperature-dependent material data from JMatPro® into the multiphase material model. Structural steels of different strengths are therefore considered. The validation experiments are carried out with a collaborative robot and a GMAW welding power source. They include the time-dependent recording of the welding parameters, the recording of the melt pool with a welding camera as well as thermography over a temperature range that takes the heat affected zone and the melted zone into account. The results will be considered with an exploratory simulation study of the damage to the welded joint in a virtual 3-point bending test.

2 Materials

For the virtual experiments in LS-DYNA we consider normalized (S420NL) and thermomechanically (S460M, S700MC) rolled as well as liquid-quenched and tempered fine-grain steels (S890Q). The formation of fine grains is essential for their strength. Depending on the type, it is supplemented by solid solution strengthening, precipitation strengthening and strengthening due to lattice transformation and dislocations. They differ significantly in terms of their yield strength and their structure before welding. Their carbon equivalent (CE) according to equation (1) is shown in Table 1.

$$CE = C\% + \frac{Mn\%}{6} + \frac{Cr\%+Mo\%+V\%}{5} + \frac{Ni\%+Cu\%}{15} \quad (1)$$

Steel grade	S420NL	S460M	S700MC	S890Q
CE	0.53	0.41	0.36	0.64

Table 1: Carbon equivalent (CE) for different fine-grain steel grades.

In the case of fine-grain steels in particular, a defined temperature control and compliance with intervals for the cooling rate is often necessary in order not to adversely change the mechanical-technological parameters of the base material because of the welding. During welding, the locally significantly different heating and cooling rates lead to phase transformations, which can usually be estimated using welding time-temperature-transformation (TTT) diagrams. In addition to a local change in the material properties, these phase transformations lead to local strains. The consideration of the phase transformation in the welding simulation is therefore necessary for these steels. For practical welding we consider the fine-grained steel S700MC. Its chemical alloy composition is shown in Table 2.

C	Si	Mn	P	S	Al	B	Cr	Cu	Mo	Nb	Ni	Ti	V
0.054	0.02	1.78	0.011	0.0032	0.034	0.0003	0.026	0.009	0.005	0.064	0.014	0.134	0.004

Table 2: Chemical alloy composition of perform® 700.

3 Validation Experiment

3.1 Experimental Setting

The validation experiment presented here is carried out on a perform® 700 type steel. This corresponds to a steel grade S700MC according to DIN EN 10149-2. The alloy composition according to the works certificate is listed in table 2. An academic component, two plates measuring 200x80x4 mm, is selected as the geometry. A UR10 robot welds the component as a butt weld in an I-joint in flat position. The welding process used is a standard gas metal arc welding (GMAW) process. The welding parameters are given in table 3 and the energy input per unit length (E) is computed according to equation (2).

$$E = \frac{U \cdot I \cdot \eta}{v} \text{ with } \eta = 0.85 \quad (2)$$

welding current	Welding voltage	Filler metal feed	Welding speed	E
287 A	28 V	8.3 m/min	10.6 mm/s	0.64 kJ/mm

Table 3: Welding parameters.

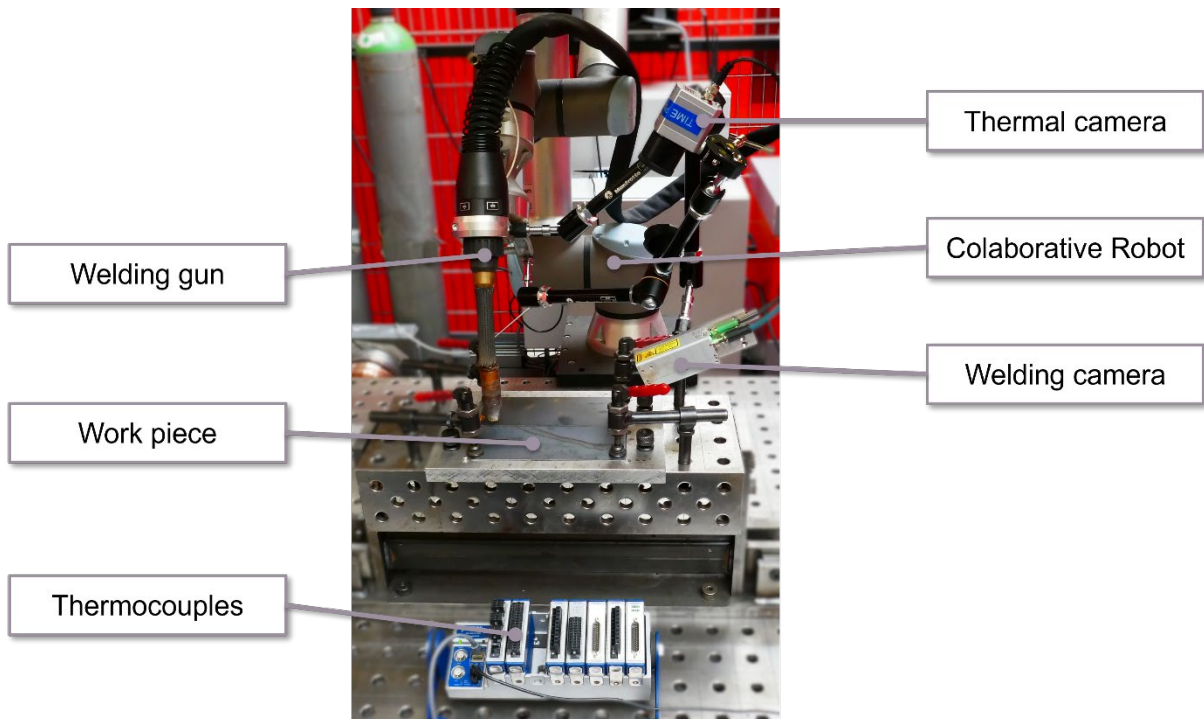


Fig.1: Experimental setting for welding.

To validate the welding simulation, we carry out temperature measurements during the experiment as shown in figure 1. We measure the temperature locally directly adjacent to the weld seam with three type K thermocouples with a measuring amplifier from National Instrument. In addition, we use an Optris PI1M thermal camera to measure temperatures between 500°C and 1800°C. This camera is particularly suitable for analyzing the high temperature gradients between the weld seam and the heat-affected zone. The visual recording of the welding process is supplemented by a Cavitax welding camera. The camera data is used to estimate the width of the weld pool in the welding simulation. Due to the camera arrangement used in this test setup, an evaluation perpendicular to the weld seam along the component surface is possible without great effort.

4 Numerical Experiments

4.1 Simulation Chain

In our contribution, we look at the welding – forming process chain. From a simulation point of view, welding is a non-linear process. The progression of the material properties is non-linear. They depend on the temperature and the phase composition and are present for a temperature interval from room temperature to the melting point. This makes it necessary to provide an extensive base of input data for the simulation. In this article, the effort is reduced by using different software systems for this.

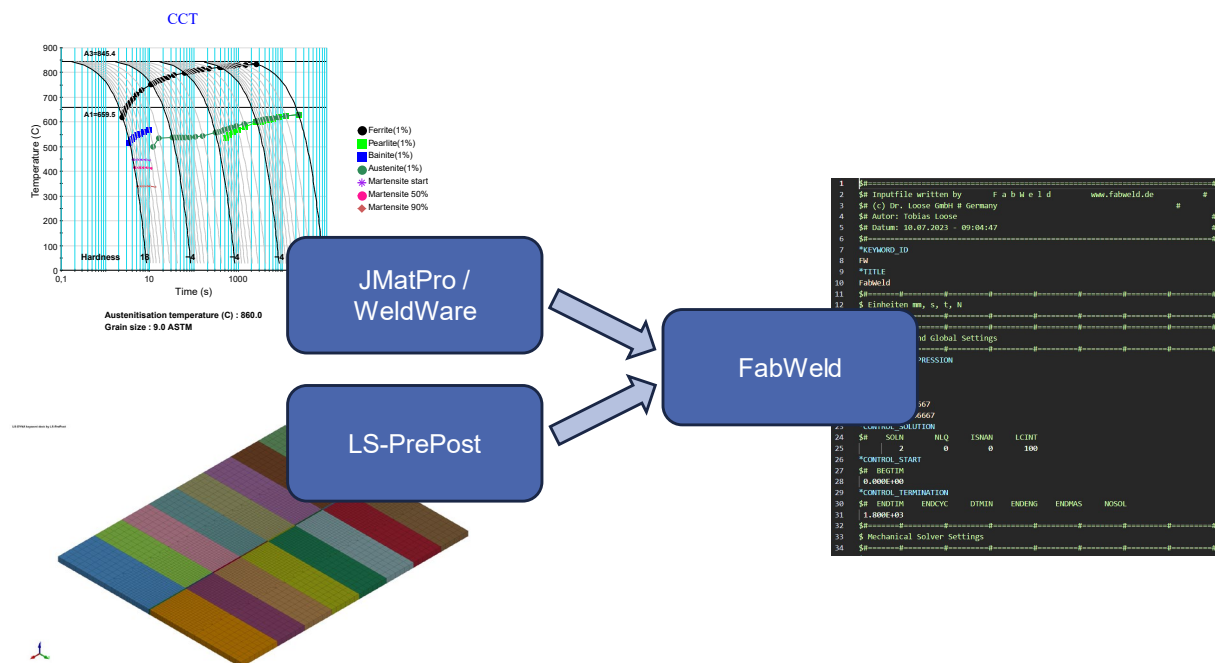


Fig.2: Used software packages for pre-processing of the welding simulation.

We use the WeldWare® software to determine the phase transformation properties and the mechanical properties at room temperature for different cooling rates including the elongation at break. With LS-PrePost we create the spatially discretized finite element model. This input data is made available to the pre-processor FabWeld®. There, the information regarding the welding process control, temporal discretization, contacts, component, and solver settings are supplemented. From this, FabWeld® creates an input script for the simulation, enables direct forwarding to the solver and post-processing tailored to the welding.

4.2 Material Simulation

The transformation properties during welding are usually estimated in practice using welding TTT diagrams. A TTT diagram calculated numerically with the JMatPro® software for the S700MC under consideration is shown at the upper left of figure 2. With WeldWare®, a welding TTT diagram is simulated for a given material with a defined alloy composition. The data and regression equations stored in WeldWare® are based on practical tests at the Welding Technical Training and Research Institute (SLV) in Rostock (Northern Germany). After entering the percentage alloy composition, the composition of the phases ferrite (F), pearlite (P), martensite (M) and bainite (B) as well as the mechanical-technological parameters hardness, yield strength, tensile strength, percentage reduction of area and percentage elongation after fracture are calculated for a related steel for the cooling time

from 850°C to 500°C (figure 3). In the case of the S700MC, we use the material type S690Q as the basis for our calculations in WeldWare®. The factory certificate at hand provides us with the chemical composition of the alloy given in table 2.

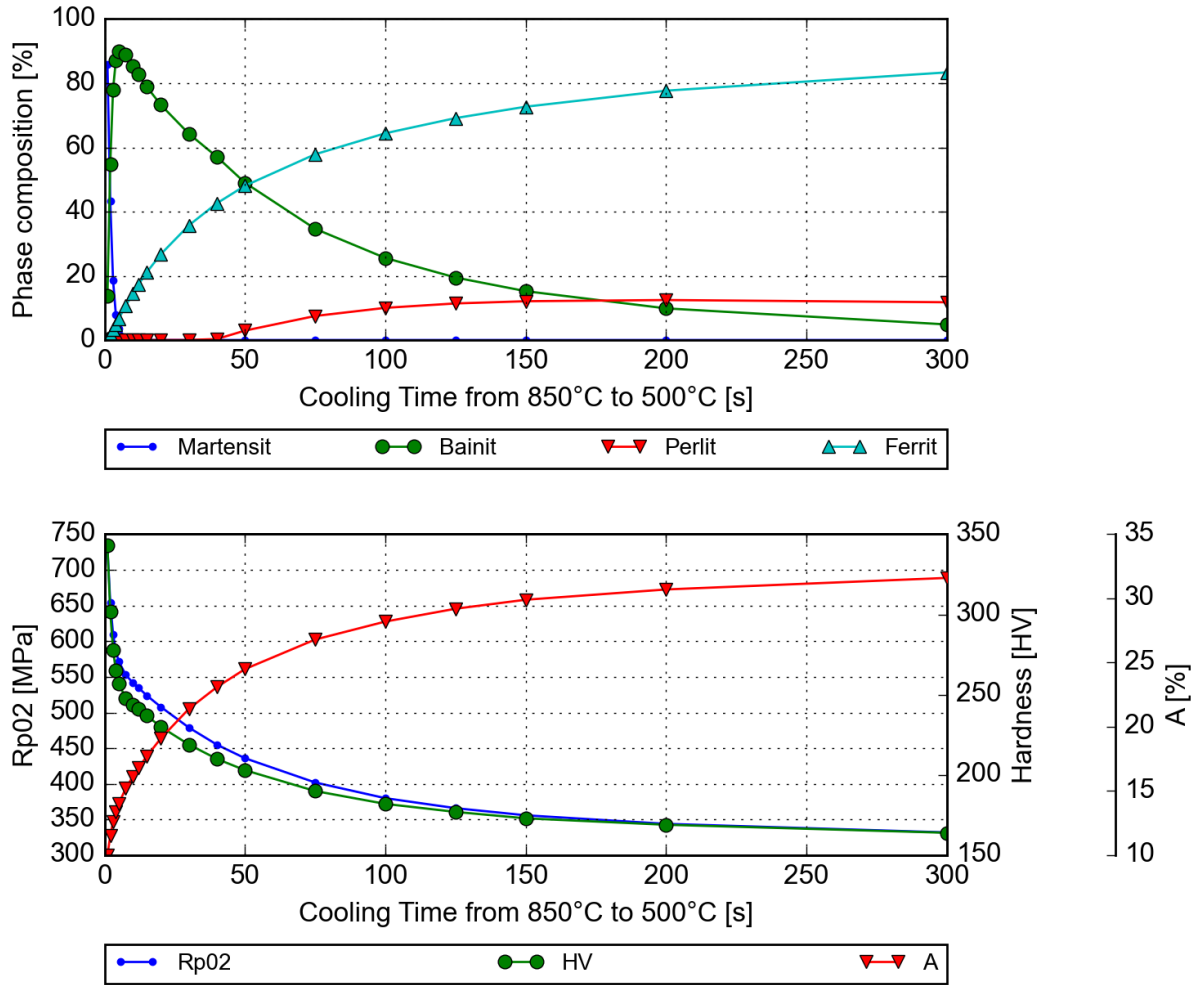


Fig.3: Phase composition and mechanical properties at room temperature for different cooling times calculated by WeldWare®.

The structured data for the present material failure strain are fitted to a multivariate regression equation using a least-squares approach according to equations (3, 4). The phases ferrite, pearlite, bainite and martensite calculated in WeldWare® are considered in the regression equation.

$$\epsilon_f = f(\%M, \%B, \%P, \%F) \quad (3)$$

$$\sum_{i=1}^N (y_i - b_0 - b_M x_{Mi} - b_B x_{Bi} - b_P x_{Pi} - b_F x_{Fi})^2 \rightarrow \min_{b_0, b_M, b_B, b_P, b_F} ! \quad (4)$$

4.3 Welding Simulation

4.3.1 Material model

To simulate the welding of a thermomechanically rolled S700MC steel, the phase transformations of the individual phases during heating and cooling are modeled using ***MAT_GENERALIZED_PHASE_CHANGE** (***MAT_254**). Up to 24 individual phases can be defined in the material card of ***MAT_254**. In our test case we use a total of 9 phases: austenite, ferrite, pearlite, bainite, martensite, base metal, filler metal, tempered bainite and tempered martensite.

The diffusion-controlled phase transformations of the phases during heating to austenite are modeled using the generalized Johnson-Mehl-Avrami-Kolmogorov (JMAK) model, which is shown in

equations (5-7). The transformation of the martensite and bainite phases into their respective tempered states is also carried out using the generalized JMAK model.

$$\frac{dx_b}{dt} = n(T)(k_{ab}x_a - k'_{ab}x_b) \left(\ln \left(\frac{k_{ab}(x_a+x_b)}{k_{ab}x_a - k'_{ab}x_b} \right) \right)^{\frac{n(T)-1.0}{n(T)}} \quad (5)$$

$$k_{ab} = \frac{x_{eq}(T)}{\tau(T)} f(\dot{T}) \quad (6)$$

$$k'_{ab} = \frac{1-x_{eq}(T)}{\tau(T)} f'(\dot{T}) \quad (7)$$

In our test case, the model is described by five parameters, of which three parameters are temperature-dependent and two parameters are dependent on the temperature change rate. The temperature-dependent exponent n is assumed to be a constant one here. Furthermore, the percentage of phases in the equilibrium state x_{eq} and the recovery time τ are given as a function of the temperature. The factors f and f' , both of which depend on the rate of temperature change, serve as correction factors. FabWeld® calculates the transformation parameters according to the given table of cooling rates and relating phase proportions.

During cooling from the austenite region, the structural transformation is divided into diffusion-controlled and non-diffusion. The diffusion-controlled transformation of austenite into ferrite, pearlite and bainite takes place using the generalized JMAK model, while the non-diffusive transformation from austenite into martensite ("flip process") takes place using the Koistinen-Marburg model according to equation (8).

$$x_b = (x_a + x_b)(1.0 - e^{-\alpha_{KM}(T_{start}-T)}) \quad (8)$$

The parameters required for both transformation laws are defined in 2D tables depending on the phases. Temperature-dependent flow curves are required for the individual phases. They are defined using approximation approach in [2]. This methodology is implemented in FabWeld® and requires the yield strength, the ultimate tensile strength, and the elongation without necking of the base metal at room temperature as input parameters.

4.3.2 Discretization and boundary conditions

The weld specimen is discretized using hexagon solids and is refined in the weld seam and the heat affected zone. Therefore, the element mesh is refined in a 3 to 1 manner for elements in the z-axis and in a 4 to 2 manner for the elements in the y-dimension along the weld path. In sum, the mesh results in 138.800 solid elements and 166.599 nodes (figure 4). The specimen is united by coincident nodes so that no contact is needed in this test case.

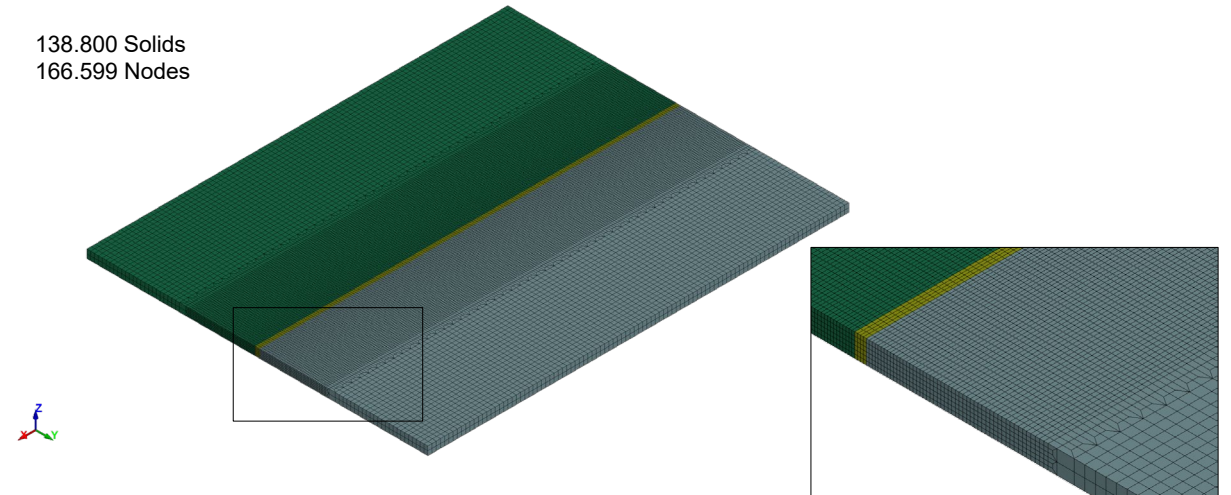


Fig.4: Spatial discretization of the weld specimen.

LS-DYNA offers the keyword `*BOUNDARY_THERMAL_WELD_TRAJECTORY` with which the welding path, the heat source type, the heat input as well as the welding speed and the heat source parameters can be defined in a compact way. In our test case we make use of an ellipsoidal heat source with constant

heat distributions for the front and the back part of the ellipsoid. The following equations (9-11) describe the heat input for the heat source [6].

$$q_i = Q f_i \frac{3}{2\pi a_i b c} \text{ with } i := \{f, r\} \tag{9}$$

$$q = q_f \text{ if } u \geq 0 \text{ and } 1 > \left(\frac{u}{a_f}\right)^2 + \left(\frac{v}{b}\right)^2 + \left(\frac{w}{c}\right)^2 \text{ else if } \tag{10}$$

$$q = q_r \text{ if } u < 0 \text{ and } 1 > \left(\frac{u}{a_f}\right)^2 + \left(\frac{v}{b}\right)^2 + \left(\frac{w}{c}\right)^2 \text{ else } q = 0 \tag{11}$$

In the following table we summarize the input parameters and its values for the heat source.

Parameter	a _f	a _r	b	c	f _f	f _r
Value	5	10	5	2	1.2	0.8

Table 4: Chosen parameters for heat input equations.

The thermal boundary conditions also take radiation and convection into account. In addition to that, we modeled the welding table with the keyword `*RIGIDWALL_GEOMETRIC_FLAT` and the local Dirichlet boundary conditions for the structural part of the simulation with `*BOUNDARY_SPC_SET` keyword. Gravity is considered via the keyword `*LOAD_BODY_Z`.

4.3.3 Results

In Figure 5, the results of the thermo-mechanical simulation are compared with the measurements of the thermal imaging camera, which recorded the temperature change with a refresh rate of 80 Hz. The three thermocouples used can also be seen on the right-hand side of the figure. Several aspects become clear here.

The emissivity between the states of aggregation "liquid" (melted material) and "solid" (solidified material) differs significantly. As a result, the temperature displayed there is incorrectly lower than it actually is. In a more detailed evaluation, the different emissivities have to be considered for precise results. Also, the area outside the weld is shown hotter due to the welding fumes and the arc being switched on. As soon as the arc is switched off, the temperatures in this area suddenly drop by around 200°C. This must be considered when evaluating the time-temperature data. The light spots in the figure represent flying sparks. In particular, the shape of the weld pool and the temperature gradient are shown in the simulation with very good accuracy.

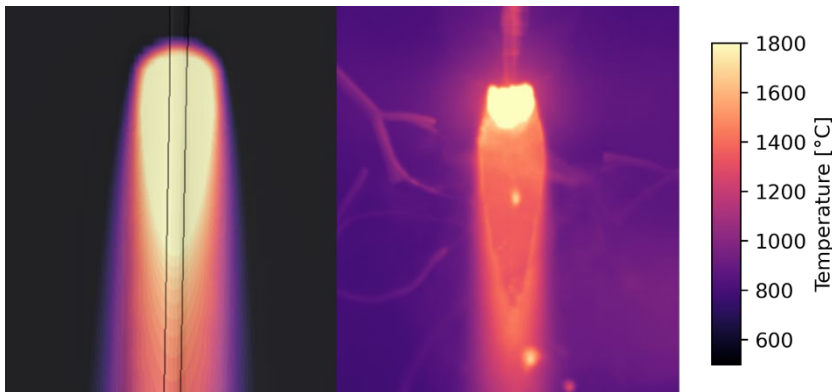


Fig.5: Comparison between simulation (left) and experiment (right).

We calculate the Vickers hardness using Blondeau's equations [9,10]. It is implemented within user defined history variables by FabWeld®. By specifying the hardness of the base material, the hardness can be visualized spatially resolved for the entire model. The hardness is calculated for the region exceeding the austenitisation. For the region without austenitisation where the base material remains unaffected the hardness is plotted as the given material property for the base material. This explains the hard drop in the heat affected zone of the weld specimen in figure 6 (lower plot).

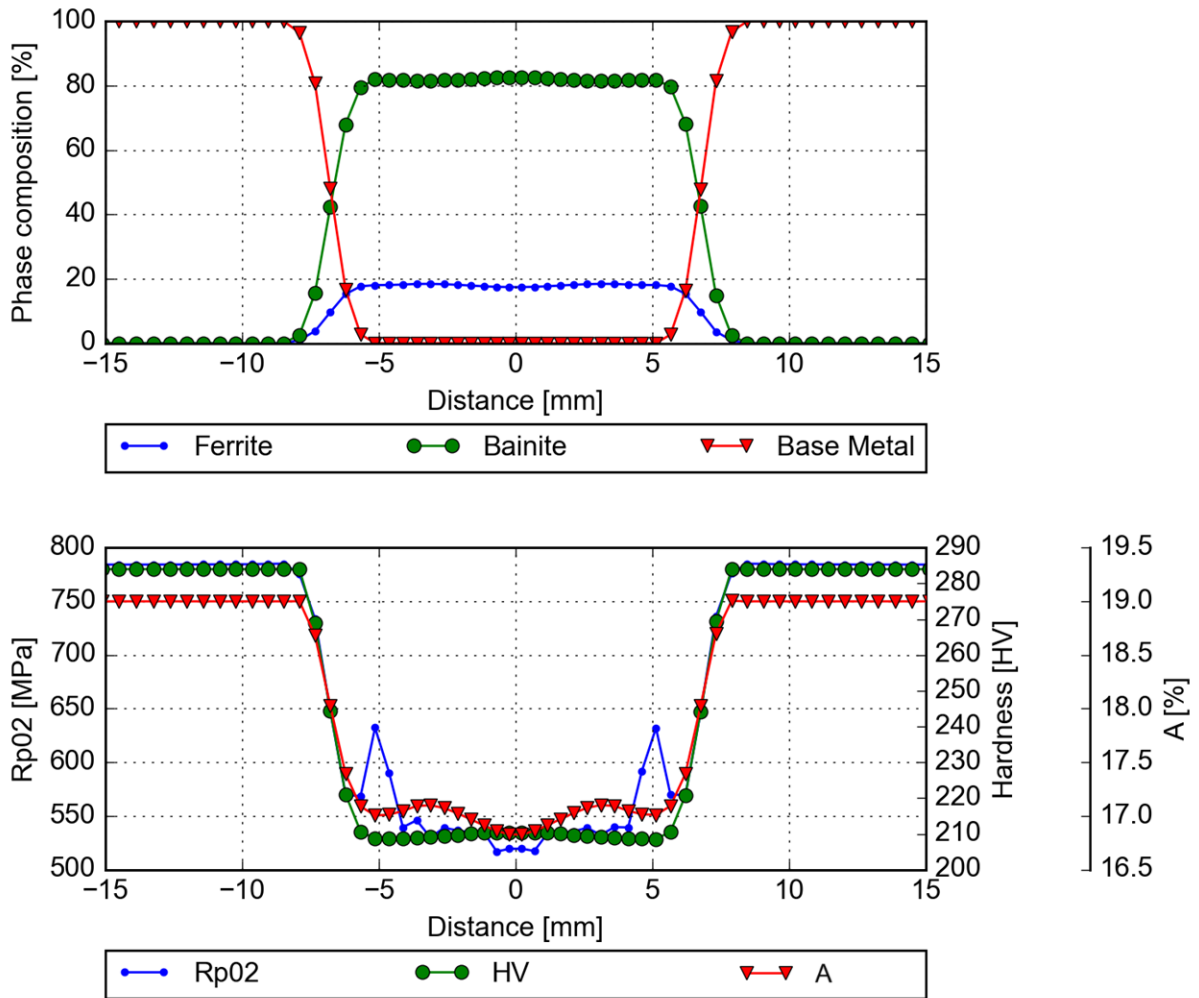


Fig.6: Phase composition and simulated mechanical properties along path vertical to the weld path.

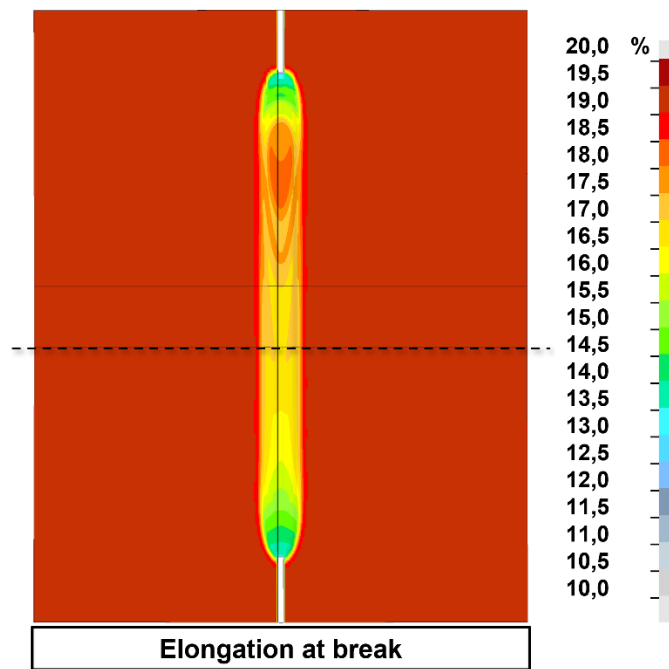


Fig.7: Elongation at break and path position.

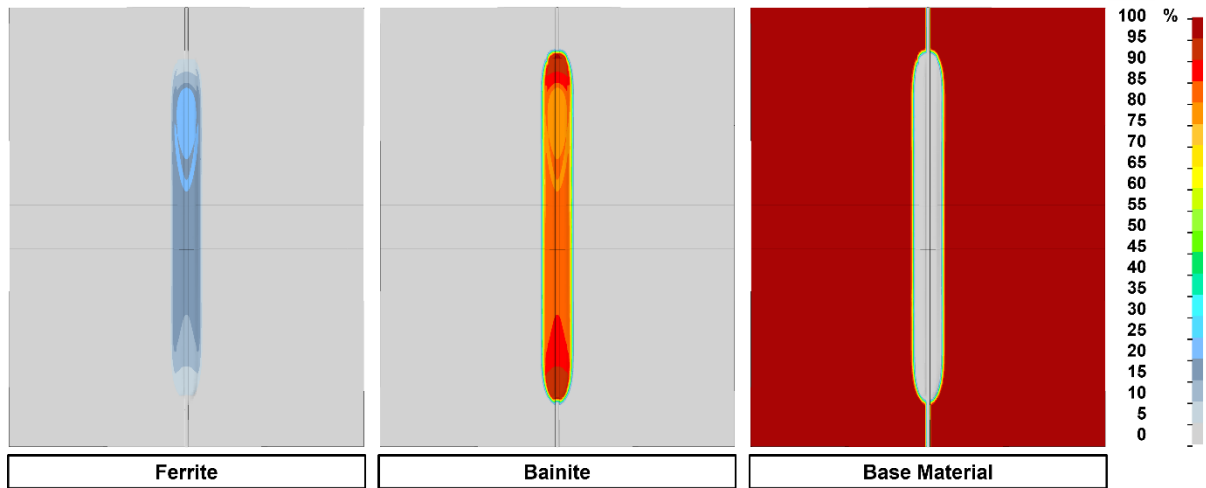


Fig.8: Phase proportion Ferrite, Bainite, and unaffected base Material

Finally, with the extension of the material model `*MAT_254` by user defined history variables, we are able to determine the metallurgical state and the state of mechanical properties after welding over the entire specimen. The phase proportion for the different phases are displayed in specimen in figure 7. The phase "base material" is the indicator of regions where the material is unaffected by heat. The region where the proportion of base material is below 100 % belongs to the heat affected zone or molten zone.

Figure 8 shows the fringe plot for yield stress, elongation at break and hardness distributed over the welded specimen. As known to the author it is the first time that elongation at break is simulated within a welding structure analysis.

5 Material modeling for bending simulation

In this paper, a first approach within the framework of the MoKaT project is presented, with which the phase-dependent modeling of the damage is carried out with the "Generalized incremental stress state dependent damage model" (GISSMO). Among other things, this is explained in detail in [7, 8]. GISSMO is a phenomenological model in which damage is described as a measure of the relative loss of extensibility and can be used via the keyword `*MAT_ADD_DAMAGE_GISSMO` in combination with other structural material models like `*MAT_254`. The damage is defined there via the degree of damage D . The increment of the equivalent plastic strain for each time step is decisive for this as shown in equation (12) [7].

$$\Delta D = \frac{nD^{1-\frac{1}{n}}}{\epsilon_f} \Delta \epsilon_p \quad (12)$$

Two parameters are important for the characterization of the material, triaxiality and lode parameter. The triaxiality η (equation (13)) relates the first invariant of the Cauchy stress tensor to the second invariant of the deviatoric part of the stress tensor. It is defined as the quotient of the hydrostatic stress and the von-Mises equivalent stress. For the plane stress state, the triaxiality is in the interval of ± 0.66 to describe the different types of loading.

$$\eta = \frac{\sigma_m}{\sigma_{vm}} \quad (13)$$

The Lode parameter ξ (equation (14)) sets the principal stresses in relation to the von-Mises equivalent stress σ_{vm} . It is defined between -1 and 1 and shows a parabolic curve for the elongation at break. For the multiaxial stress state of 3D solid elements, the elongation at break is given as a function of the lode parameter and the triaxiality.

$$\xi = \frac{27}{2} \frac{J_3}{\sigma_{vm}^3} \quad (14)$$

The material card also offers the possibility of modeling other dependencies for the elongation at break. For example, the dependency on the temperature for history variable 1 is preconfigured. This option is used to transfer the results of the welding simulation with the multi-phase material card ***MAT_254** along the process chains welding - forming or welding - crash. In ***MAT_ADD_DAMAGE_GISSMO** we define a dependence of the elongation at break on a user-defined history variable (equation (15)). This history variable is our elongation at break calculated during the welding simulation and dependent on the percentage phase composition. The approach is therefore to scale the elongation at break-triaxiality curve of the base material as a function of the phase composition using a rule of mixtures.

$$\epsilon_f^p = \epsilon_f^p(\eta, \%M, \%B, \%P, \%F) \quad (15)$$

For our virtual tests of the GISSMO material card, we initially use user defined values for the curve of the elongation at break depending on the triaxiality as a basis. Given the value of the elongation at break for a uniaxial tensile stress (triaxiality = 0.33), we scale the entire curve to the value of the elongation at break of the parent metal. The other parameters are set like in table 5 at this time.

Parameter	dtyp	refsz	numfip	dmgexp	dcrit	fadexp	lcregd	shrf	biaxf
Value	1.0	0.0	1.0	2.0	1.0	2.5	0	1.0	1.0

Table 5: Input parameters for ***MAT_ADD_DAMAGE_GISSMO**

Furthermore, we use the calculation results from WeldWare® for the elongation at break. They are available as pairs of values for elongation at break and phase composition. We also scale the base curve for these elongation at break values. As an interim result, we have a family of curves for different elongation at break values for uniaxial tensile stress.

We create a 3D table for all these elongation at break values, which are also the support points of the regression equation (4) and refer to 2D tables of the lode parameter in each case. Since we do not yet consider the lode parameter explicitly, the elongation at fracture triaxiality curve is constant between -1 and 1 for each lode parameter. Each 2D table in turn references the scaled curve of the elongation at break as a function of triaxiality.

After the simulation of the welding process, we receive the elongation at break in a spatially resolved manner and can thus define the material card ***MAT_ADD_DAMAGE_GISSMO** as a function of the elongation at break which is phase dependent. In figure 9 one can see the full break of the bending probe due to a three-point bending with rigid cylinders and the resulting contact force in z-direction over time between the bending probe and the smaller cylinder. The steps in the force plot correlate with element deletions during the simulation.

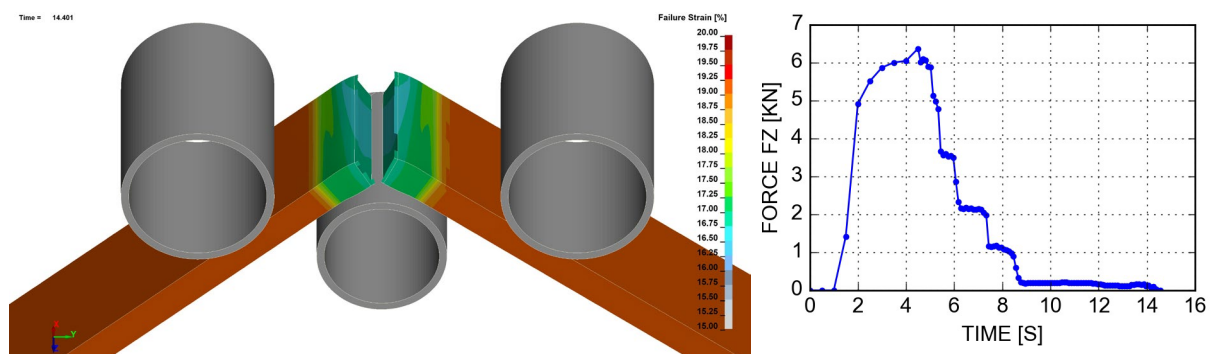


Fig.9: Bending sample and rigid cylinders after full break (left) with contact force reaction over time (right).

6 Outlook

The first approach presented here for the prediction of component failure under the influence of the phase composition after welding needs to be validated by physical tests. According this validation of the model, it has to be checked if an extension of the model is needed to get more precise prediction results.

7 Acknowledgement

We would like to thank the German Federal Ministry of Economics and Climate Protection, which is currently funding the MoKaT project as part of the Central Innovation Program for SMEs (ZIM).

8 Summary

In this article, we presented a first approach based on welding experiments, welding simulations and bending simulations to model the multi-phase microstructure after welding in the simulation of the welding-forming or welding-crash process chains.

Based on a material simulation of the elongation at break depending on the phase composition, welding simulations were carried out with the material model ***MAT_GENERALIZED_PHASE_CHANGE** and the elongation at break depending on the phase composition for the welded component was calculated. The spatially resolved elongation at break was used as an input variable for subsequent simulations with the material model ***MAT_ADD_DAMAGE_GISSMO** and was defined in 3D tables. The workflow for a process chain using the example of welding and bending was presented in this article.

9 Literature

- [1] Goldak, J.A., Akhlaghi, M.: "Computational Welding Mechanics", Springer, Boston, MA, 2005, ISBN: 9780387232874
- [2] Loose, T.: "Einfluß des transienten Schweißvorganges auf Verzug, Eigenspannungen und Stabilitätsverhalten axial gedrückter Kreiszyinderschalen aus Stahl", 2007
- [3] Hildebrand, J.: "Numerische Schweißsimulation - Bestimmung von Temperatur, Gefüge und Eigenspannung an Schweißverbindungen aus Stahl- und Glaswerkstoffen", 2008
- [4] Loose, T., Klöppel, T.: "A LS-DYNA material model for the consistent simulation of welding, forming and heat treatment", 11th International Seminar Numerical Analysis of Weldability, Seggau, Austria, 2015, <https://dr-loose-gmbh.de/onewebmedia/2015-Seggau-Material.pdf>
- [5] Loose, T., Girresser, T., Goldak, J.A.: "Validation of Welding Structure Simulations", 13th International Seminar Numerical Analysis of Weldability, Seggau, Austria, 2022
- [6] Loose, T., Rohbrecht, J.: "Equivalent energy method for welding structure analysis", Welding and Cutting 17, No. 3, 2018
- [7] Basaran, M.: "Stress State Dependent Damage Modeling with a Focus on the Lode Angle Influence", 2011
- [8] Neukamm, F.: "Lokalisierung und Versagen von Blechstrukturen", 2018
- [9] Blondeau, R., Maynier, Ph., Dollet, J.: "Forecasting the hardness and resistance of carbon and low alloy steels according to their structure and composition", Mem. Sci. Rev. Metallurgie, No. 12, 1973
- [10] Blondeau, R.; Maynier, Ph., Dollet, J., Vieillard-Baron, B.: "Forecasting the hardness and resistance of carbon and low-alloy steels according to their composition and heat treatment", Mem. Sci. Rev. Metallurgie, No. 11, 1975

Gefördert durch:



Bundesministerium
für Wirtschaft
und Klimaschutz

aufgrund eines Beschlusses
des Deutschen Bundestages

